Journal of Evolving Space Activities
Vol. 3, Article No. 225, 2025
DOI: 10.57350/jesa.225

Flame response of a sub- and supercritical LOX/H_2 and LOX/LNG rocket combustor with large optical access*

Jan MARTIN,[1)†] Wolfgang ARMBRUSTER,[1)] Michael BÖRNER,[1)] Justin HARDI,[1)] and Michael OSCHWALD[1),2)]

[1)] *Institute of Space Propulsion, German Aerospace Center (DLR), 74239 Lampoldshausen, Germany*
[2)] *Institute of Jet Propulsion and Turbomachinery, RWTH Aachen University, 52062 Aachen, Germany*

(Received July 5th, 2023)

Hot fire tests including flame radiation and acoustic measurements were performed in a single-element rocket combustor with large optical access (255x38 mm) for sub- and supercritical injection conditions. Three test campaigns were conducted with the propellant combination of liquid oxygen and hydrogen (LOX/H_2), liquid oxygen and compressed-natural-gas (LOX/CNG), as well as liquid oxygen and liquefied natural gas (LOX/LNG) at conditions relevant for main- and upper-stage rocket engines. High-speed imaging of the flame in blue radiation wavelengths (capturing CH* when natural gas was the fuel) was conducted. For the analysis of the flame-acoustic interaction, these measurements are related with the interpolated acoustic pressure distribution in the chamber.While three load points (LPs) feature high-amplitude, self-sustaining oscillations of the longitudinal acoustic resonance modes, one LP is intermittently unstable and two LPs are stable. Three different regions of interest (ROIs) were used to calculate flame transfer functions (FTFs) from the 2D imaging data, each increasing successively in their extent. While the phase difference between the radiation intensity and acoustic pressure is consistent for all three ROIs, the gain values differ. The largest ROI including the complete extent of the optically accessible region provided gain values qualitatively most consistent with expected distributions.

Key Words: Rocket Engine, Subcritical Combustion, Supercritical Combustion, Optical Access, Liquid Oxygen / Natural Gas, Liquid Oxygen / Hydrogen, Single-Injector

Nomenclature

$\dot{q}'$	:	heat release rate
p'	:	unsteady pressure
d	:	diameter
l	:	length
T	:	temperature
P	:	pressure
h	:	height
ROF	:	ratio of oxidizer to fuel mass flow rate
ROI	:	region of interest
UV/OH*	:	radiation in the ultraviolet wavelengths, including emissions of the OH* radical
BR/CH*	:	radiation in the ultraviolet wavelengths, including emissions of the CH* radical with hydrocarbon fuels
CWL	:	center wavelength
FWHM	:	full width at half maximum
LP	:	load point; set of operating conditions
H_2	:	Hydrogen
CNG	:	compressed-natural-gas
LNG	:	liquefied-natural-gas
Subscripts		
o	:	oxidizer, here liquid-oxygen
f	:	fuel
t	:	nozzle throat
cc	:	combustion chamber
c	:	cooling, here compressed-natural-gas

†Corresponding author, jan.martin@dlr.de

1. Introduction

Liquid-propellant rocket engines (LPREs) are a key technology of most launcher propulsion systems. The occurence of high-frequency combustion instabilities imposes a high risk on the safe operation of LPREs. The Rayleigh-Criterion provides a theoretical foundation for thermoacoustics driving, which can lead to combustion instabilities.[5)] If pressure oscillations (p') are in phase with heat release oscillations ($\dot{q}'$) the necessary condition for growing amplitudes is met. Understanding the interaction of the combustion and chamber acoustics is crucial for identifying and eliminating the risk of occurrence of combustion instabilities. The mathematical description of this criterion is given in Eq. 1.

$$\int_0^T \int_V p'(\vec{x},t)\dot{q}'(\vec{x},t)dVdt > 0 \tag{1}$$

The prediction of combustion instabilities stays a challenging topic even though the chamber acoustics itself are theoretically well understood. One important aspect in predicting this unwanted combustion behavior in LPREs is the description of the flame response to mass flow (velocity) or pressure oscillations. Functions describing the frequency dependent heat release response are referred to as flame transfer functions (FTFs) and can be applied in low-order models.[6,7)] FTFs are usually defined as normalized integrated heat release rate oscillations $\dot{Q}'$ in response to p'[8,9,31)] (Eq. 2) or more often in response to acoustic velocity (u')[10–12,25,32)]

$$FTF(\omega) = \frac{\dot{q}'(\omega)/\bar{\dot{q}}}{p'(\omega)/\bar{P}} \quad (2)$$

A shortcoming in the experimental determination of FTFs is that no direct measurement of the heat release rate is possible. In former studies regarding flame-acoustic interaction in LPRE combustion OH* radiation measurements have been used as a marker for heat release rate.[14,15,31] Recent investigations[16,17] reveal that UV radiation suffers from high self-absorption at pressures relevant for most LPREs. The measured intensity is dominated by emission closest to the observer.[17] Further limitation is given at temperature above 2700 K,[17] where OH* emission is driven rather by thermal excitation than chemiluminescence. Thus no direct relation between its measurement and $\dot{q}'$ is given. Investigations regarding the blue region of the O_2-H_2 spectrum[16,17] in hydrogen combustion and CH* emission in methane combustion suggest that blue radiation does not suffer from this shortcoming and therefore is a better marker for time resolved heat releases under such conditions.[18] Although there is a lack of an established proportionality between line-of-sight integrated radiation measurements and $\dot{q}'$, neither for blue nor OH* wavelengths,[16] previous experiments with this experiments showed their potential as qualitative markers for heat release.[19]

However, the FTFs of a injection element can be extracted from cost-effective sub-scale single-injector experiments. The implementation of the experimental FTFs in appropriate low-order models can be able to predict the likelihood of combustion instabilities in the full-scale engine. Therefore, the application of FTFs in combination with low-order models can be a useful, low-resources, and fast approach for the assessment of the potential of thermoacoustic instabilities in the development process of rocket engines.

The experimental DLR rocket combuster model 'N' (BKN), with its large optical access, enables the investigation of a great portion of the flame's behavior in response to a wide range of operating conditions. An examination of the 2D-Rayleigh-Index spectra for different sets of operating conditions (load points; LPs) has been previously conducted.[19] The present work aims to derive flame transfer functions for the same operating conditions and discuss these with respect to the 2D-Rayleigh-Index spectra and experimental conditions.

First the experimental setup in terms of a brief description of BKN, the optical diagnostics and the operating conditions are presented. Then the methodology of the performed analysis will be described. Finally the results of this analysis will be presented and discussed.

2. Experimental Method

2.1. Combustion Chamber

In the framework of the presented tests BKN consisted of a single-element injector, an optical chamber segment with 50 mm diameter, up to three additional chamber segments and a convergent divergent nozzle. A schematic of the experimental hardware including the instrumentation as well as

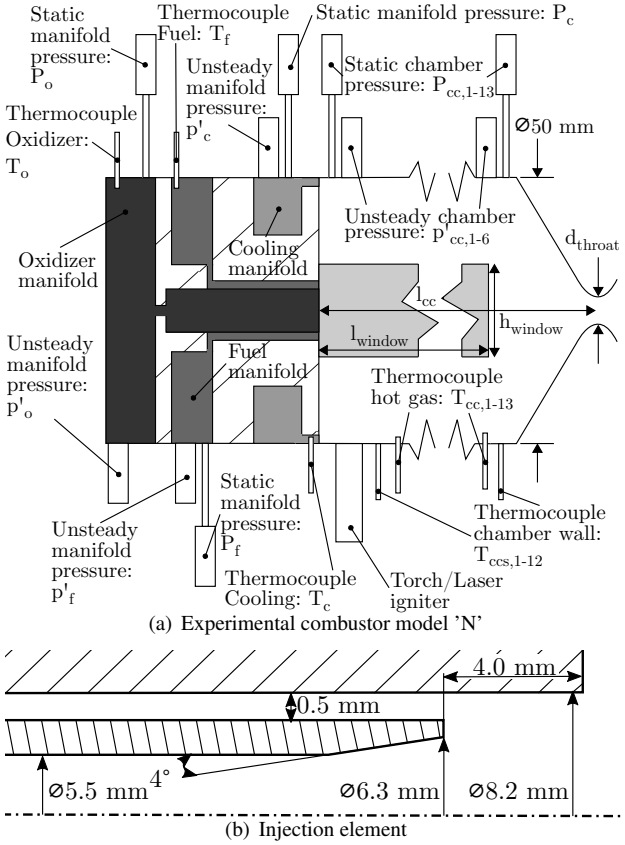

Fig. 1. Combustor and injection element schematics[27]

injection element is illustrated in Fig.1. The shear coaxial injection element features a tapered and recessed LOX post (Fig. 1(b)). The throat diameter of the nozzle (d_{throat}) measured 14.5 mm. The length of the combustor (l_{cc}) from faceplate to the nozzle throat with a diameter was varied between 359, 429, 539 and 609 mm. The dimensions of the optically accessible region are 253.5 mm in length (l_{window}) and 38 mm in height (h_{window}).

A detailed description of the experiment has been provided in previous publications about experiments with gaseous hydrogen,[20] CNG[21] or LNG[19] as fuel. At least one temperature measurement with a sampling rate of 100 Hz and a static pressure measurement with a sampling rate of 1000 Hz were available in the LOX manifold (T_{o},P_{o}) and fuel manifold (T_{f},P_{f}) to determine the thermodynamic state of the fluids. For acoustic measurements, six flush mounted, unsteady pressure sensors ($p'_{\text{cc,1-6}}$) are axially distributed at distances of 34.5, 84.5, 94.5, 134.5, 164.5 and 234.5 mm downstream of the faceplate. The signals are sampled at a rate of 100 kHz with a 30 kHz second order anti-aliasing filter and have a measurement range of ±30 bar. The hot-fire tests presented in this work were conducted at the European Research and Technology Test Facility P8 for cryogenic rocket engines.

2.2. Optical Diagnostics

High-speed imaging of the ultraviolet (UV/OH*) and blue optical regime (BR/CH*) was carried out using two, synchronous high-speed cameras coaxially orientated with the same field of view recording between 2000-20000 frames per second (fps). A dichroic mirror (transparent for visible light and reflective for UV radiation) split the optical axis for ob-

Table 1. Operating conditions

LP	P_{cc}	ROF	1L Frequency	Stable
2,H_2	64.3 bar	5.8	2425 Hz	✓
1,CNG	66.8 bar	2.8	1310 Hz	✓/✗
1,LNG	62.9 bar	3.5	815 Hz	✗
2,LNG	65.4 bar	3.0	806 Hz	✗
3,LNG	41.3 bar	3.4	920 Hz	✗
4,LNG	40.5 bar	2.5	830 Hz	✓
Uncertainty	±1.1%	±5%		

taining an identical field of view for both camera systems. The filters are specified by a center wavelength (CWL) of 310 nm for OH* and 436 nm for CH* radiation, both with a full width at half maximum (FWHM) of 10 nm.

2.3. Operating Conditions

Data from six load points (LPs) originating from four different test runs in three different campaigns are discussed in detail in this work. The first LP (2,H_2) during stable combustion from the first test campaign with hydrogen (H_2) as fuel is at a chamber pressure (P_{cc}) of 64.3 bar and ratio of oxidizer to fuel (ROF= $\frac{\dot{m}_o}{\dot{m}_f}$) at the main injector of 5.8. The second LP (1,CNG) features compressed-natural-gas as fuel and intermittent excitation of the chamber longitudinal resonance (L-) modes at a P_{cc} of 66.8 bar and ROF of 2.8. Finally in the remaining four LPs CNG was mixed with liquefied-natural-gas (LNG) at chamber pressure values between 40.5 and 65.4 bar and ROFs between 2.5 and 3.5. The subcritical LP with P_{cc} of 40.5 bar and ROF of 2.5 is characterized by stable combustion while the other three LPs from this campaign are characterized by self-sustaining high-amplitude combustion instabilities of the L-modes. The operating conditions including the combustion stability behavior are summed up in Table 1. High-speed imaging of OH* and in the blue radiation wavelengths (including CH* for hydrocarbon combustion) with 13.5 kfps for LP1,LNG and LP2,LNG and 20 kfps for LP2,H_2, LP1,CNG, LP3,LNG and LP4,LNG is available. While the chamber pressure is above the critical pressure with respect to oxygen and hydrogen/methane (supercritical) for LP2,H_2 to LP2,LNG, this is not the case for LP3,LNG and LP4,LNG (subcritical).

3. Methodology

3.1. Decomposition and reconstruction of dynamic data

A multi-variable implementation of dynamic mode decomposition (DMD) following Beinke[31] was used to analyze high-speed imaging data. Resampling additional sensor data to the snapshots of high-speed imaging and adding those as pseudo-pixels to the DMD enables a more straightforward analysis of imaging in relation to sensor data. Performing the DMD on this data isolates the underlying dynamics in the data to its frequencies, here the flame imaging and sensor measurements. Afterwards the matrix containing the spatial data of each mode is divided again in the imaging and sensor data. Thus each type of measurement can be treated individually but is filtered to modes containing the same frequency content. This method allows to investigate the reconstructed flame dynamics, the pressure oscillations and their phase relationship in the chamber at frequencies of interest.

The decomposed pressure oscillations gained from the DMD are used to reconstruct the pressure field in the chamber. A spline-interpolation method is used to reconstruct a 1D-pressure distribution between faceplate and nozzle throat with the additional condition of zero pressure gradients at both ends, but also at the chamber walls. Due to the analysis of a single injection element in this work, a uniform pressure field at any radial position within the chamber is assumed and the 1D-pressure distribution is extended to the whole chamber.

3.2. Flame dynamics analysis

The decomposed and reconstructed data offers various opportunities to investigate flame-acoustic interaction. First the dynamic behavior of the flame itself can be easily analyzed by recombining the spatial data of the decomposed images with the temporal data. However, this work focused on combined (intensity and pressure) reconstructions. The radiation in the blue wavelengths was found to be optically thin compared to the radiation in the ultraviolet regime due to a higher ratio of excited to ground state concentrations for the CH* radical. Furthermore a shorter duration of the peak CH* concentration improves the suitability of CH* as a marker for time-resolved heat release.[18] Although these findings were observed at subcritical pressure conditions and for supercritical pressure conditions, the spectrum shows a strong influence of the continuum emission around 430 nm .[28] Nevertheless, a previous work showed the qualitative suitability of CH* as a marker for heat release above this validated range.[19] Therefore, the radiation in the blue wavelengths is used as an intensity measurement in this work.

Combinations of both data sources enables the calculation of a 2D Rayleigh-Index via Eq. 3 for each (or multiple) frequencies referring to the decomposed mode(s) m.

$$RI(x,r) = \sum_{\mathrm{m}} (|p'(x,r,f(m))||I'(x,r,f(m))| \cos(\Theta_{\mathrm{p'-I'}}(x,r,f(m)))) \tag{3}$$

Here I' denotes the fluctuating part of the captured intensity, p' the pressure oscillations and $\Theta_{\mathrm{p'-I'}}$ the phase difference (according to Eq. 4) between those signals for each pixel in dependency of the reconstructed mode and thus the frequency.

$$\Theta_{\mathrm{p'-I'}}(x,r,f(m))) = \Theta_{\mathrm{p'(x,r,f(m))}} - \Theta_{\mathrm{I'(x,r,f(m))}} \tag{4}$$

A normalized 2D gain of the flame to the local pressure fluctuations can be calculated according to Eq. 5 (based on Eq.2).

$$n(x,r,f(m)) = \frac{|I'(x,r,f(m))|/\bar{I}}{|p'_{\mathrm{cc},1}(x,r,f(m))|/P_{\mathrm{cc}}} \tag{5}$$

While the fluctuating portion of the intensity is normalized by the mean intensity value $\bar{I}$, the acoustic pressure fluctuations are normalized by the mean chamber pressure P_{cc} in the corresponding evaluation interval. If either the reconstructed or the raw data in the time domain is reduced to 1D signals an experimental FTF can be calculated according to Vold et al.[22] dividing the cross-spectral density (CSD) of input (here

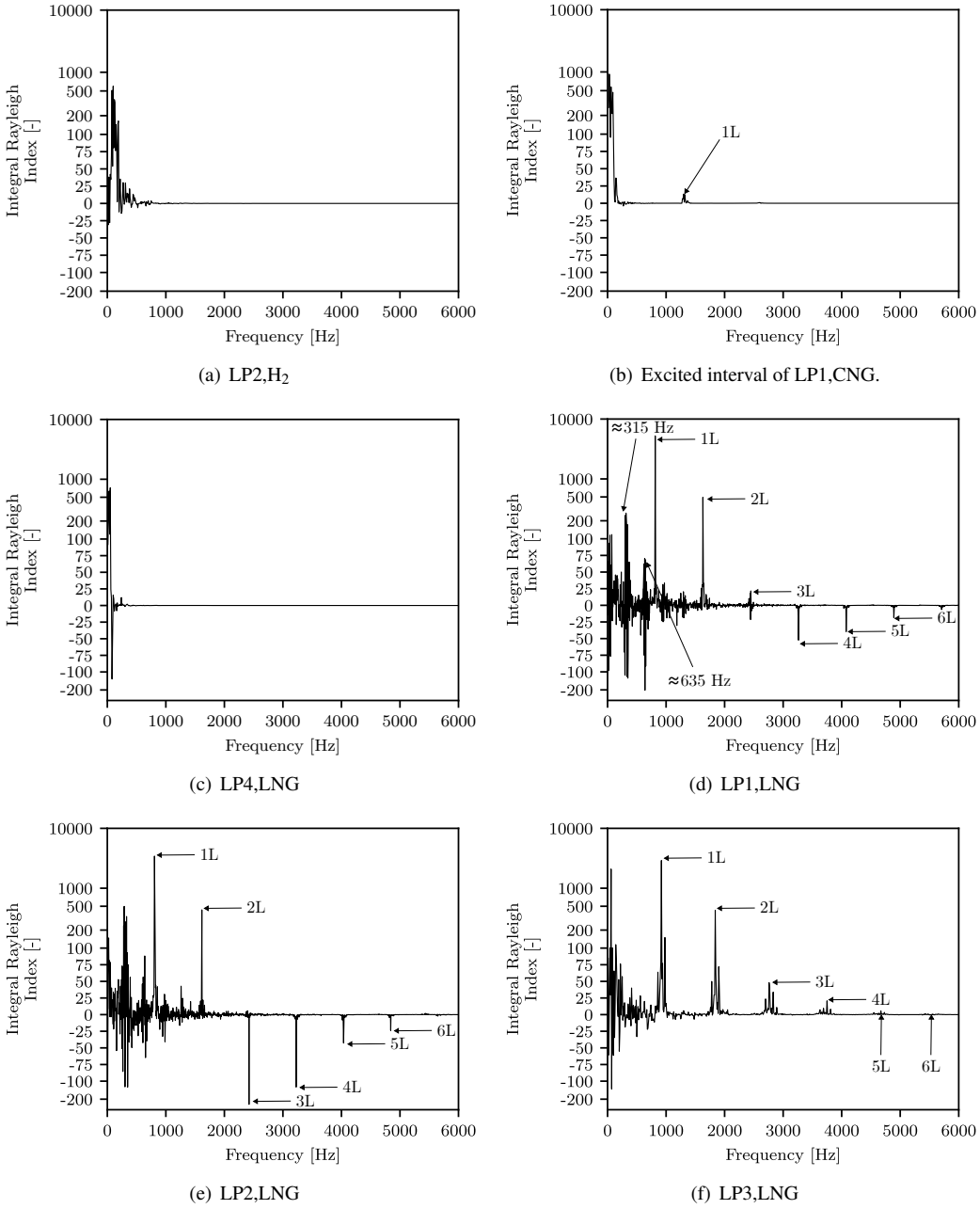

(a) LP2,H_2 (b) Excited interval of LP1,CNG.

(c) LP4,LNG (d) LP1,LNG

(e) LP2,LNG (f) LP3,LNG

Fig. 2. Integral Rayleigh Index spectra. Note that the y-axis scale is linear below absolute values of 100 and logarithmic above.[19)]

unsteady pressure) and output signal (here intensity fluctuation) by the power spectral density (PSD) of the input signal (Eq. 6).

$$FTF(\omega) = \frac{CSD(p'_{cc,1}(t)/P_{cc}, I'(t)/\bar{I})}{PSD(p'(t)/P_{cc})} \tag{6}$$

4. Results and Discussion

4.1. Flame Response

First the flame response will be presented in form of integral Rayleigh indices. These indices are obtained by integrating the 2D Rayleigh index distribution (according to Eq. 3) over the entire optical accessible region for each mode. The Rayleigh Index spectra for all six LPs are shown in Fig. 2. It was found in a previous publication that these reflect the thermodynamic state of the combustor.[19)]

LPs H_2 (LP2,H_2; Fig. 2(a)) and LNG (LP4,LNG; Fig. 2(c)) with stable combustion exhibit almost no response of the flame radiation throughout the majority of the frequency spectrum. Positive values are observed in the low frequency range where broadband combustion noise is always present. However, LP1,CNG shows a different picture during an interval characterized by an intermittent excitation of the chamber's first longitudinal resonance mode (1L mode) Fig. 2(b)). Here, a minor positive flame response can be seen. The LPs with high amplitude instabilities show a strong flame response, especially in the vicinity of the chamber eigenmodes. The supercritical LP1,LNG (Fig. 2(d)) and LP2,LNG (Fig. 2(e)) have a positive value of the Rayleigh Index for the first two eigenmodes and a negative value for the third mode

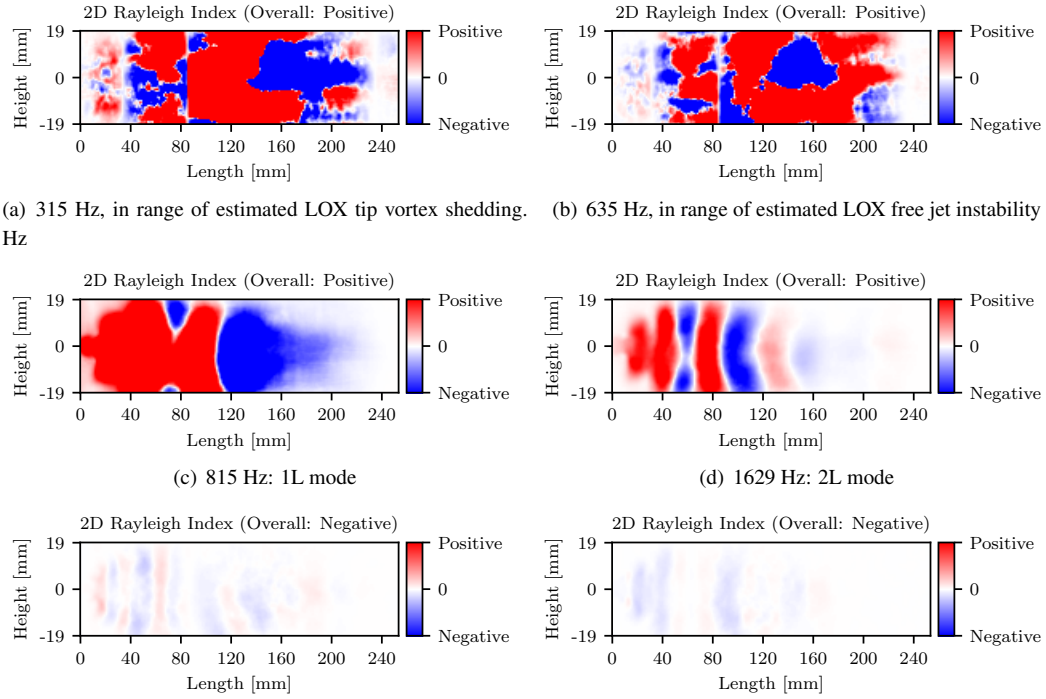

(a) 315 Hz, in range of estimated LOX tip vortex shedding. Hz

(b) 635 Hz, in range of estimated LOX free jet instability

(c) 815 Hz: 1L mode

(d) 1629 Hz: 2L mode

(e) 2444 Hz: 3L mode

(f) 3263 Hz: 4L mode

Fig. 3. 2D Rayleigh-Index distribution at various frequencies for LP1, LNG.

and above. On the other hand, the subcritical LP3,LNG, shows strong positive responses for all observable frequencies near the chamber eigenmodes. A possible explanation could be that the flame response may differ for sub- and supercritical conditions due to the well-known differences in atomization and mixing characteristics for the regimes. However, further investigation is required to seek a physical explanation for this observation.

2D-Rayleigh-Indices provide information about the spatial distribution of regions with intensified flame response. This information can provide insight about the regions that contribute most to the integral Rayleigh-Index and can indicate potential coupling mechanisms. Fig. 3 visualizes the 2D-Rayleigh-Index distributions for the most prominent frequencies of the Rayleigh-Index spectra for LP1,LNG (Fig. 2(d)). It should be noted that the color axis limitations for Fig. 3(a) and Fig. 3(b) were lowered to emphasize the near injector region, resulting in over-saturation further downstream.

Fig. 3(a) shows the first strong response in the Rayleigh-Index spectra at a frequency of 315 Hz. Since the LOX post's first longitudinal resonance frequency under these conditions is estimated to be approximately at 2.7 kHz, this cannot be the source of this observation. The derivation of Strouhal numbers based on the geometrical dimensions in the injection system indicates that this frequency falls within the range where vortex shedding is likely to occur at the backward-facing step of the LOX post tip.[29] The 2D-Rayleigh-Index representation at this frequency displays a counter-phased distribution above and below the center of the optical accessible region near the injection plane. This indicates a rotating vortex shedding at the LOX post tip and thus a helical structure on the LOX jet.

The 2D-Rayleigh-Index at 635 Hz is provided in Fig. 3(b). Again, an acoustic LOX-post-coupling can be excluded. Strouhal number correlations suggest that this frequency band may be linked to free jet instabilities[30] of the LOX jet. Support for this hydrodynamic phenomenon is provided by the 2D-Rayleigh-Index. Here, phase-symmetrical structures with respect to the center-line are visible in the near injector region. A downstream propagation of this LOX jet perturbations is indicated by the alternating blue and red structures. The development of combustion instabilities are recognized to be often linked to hydrodynamics processes.[29]

During the high-amplitude combustion instabilities of LP1,LNG both mechanisms are active and in phase with the acoustic pressure oscillations in the near injector region which is know to play a major contributing role to the combustor (in-)stability.[9,33] The hydrodynamics may, therefore, affect the thermoacoustic behavior of the combustor and contribute to deveveloping and sustaining the high-amplitude combustions instabilities noticed for LP1,LNG to LP3, LNG.

Fig. 3(c) shows the 2D-Rayleigh-Index for the 1L mode of the chamber, which provides the highest peak in the Rayleigh-Index spectra (Fig. 2(d)). In addition to a strongly positive overall index, it can be seen that nearly the whole flame zone is positively coupled with the acoustic pressure oscillations. This shows that the reaction rates for the combustion of LOX and natural gas under these operating conditions favor a positive feedback-loop between the pressure oscillations and the heat release fluctuations. This positive feedback loop is a necessary condition for thermoacoustic instabilities to grow and be sustained according to the Rayleigh criterion (Eq.1).

The 2L mode in Fig. 3(d) draws a similar picture, albeit with weaker but still positive coupling compared to the 1L mode. Also the results of the 3L mode and th 4L mode are in line with the Rayleigh-Index spectra for this LP (Fig. 2(d)). While the overall Rayleigh-Index is neutral or slightly posi-

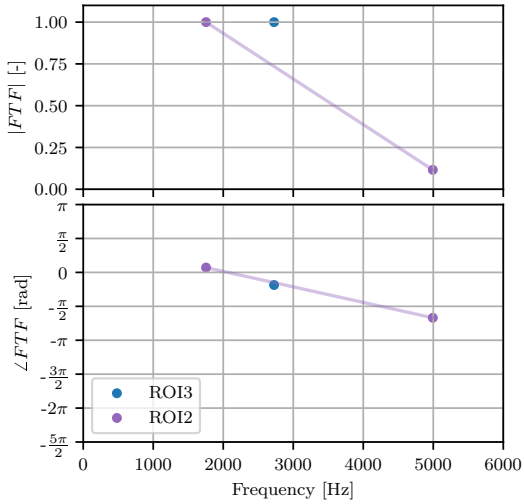

(a) LP2,H_2

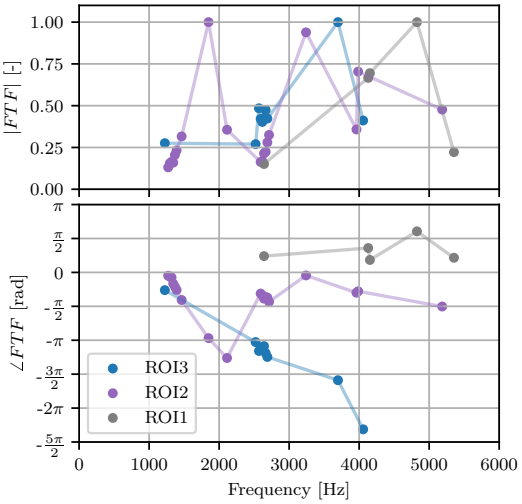

(b) Excited interval of LP1,CNG

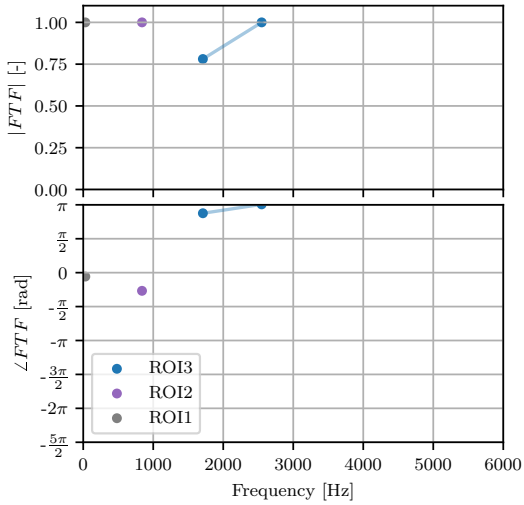

(c) LP4,LNG

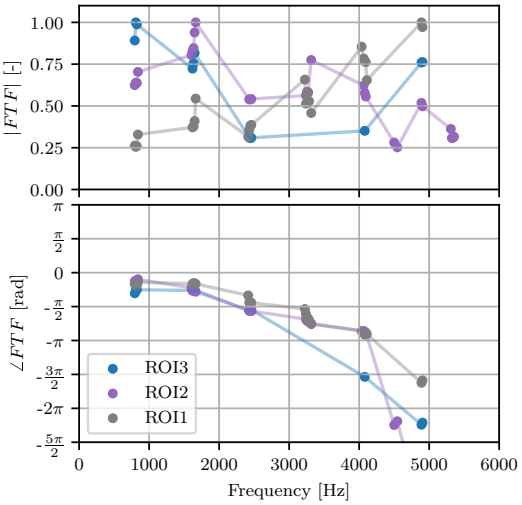

(d) LP1,LNG

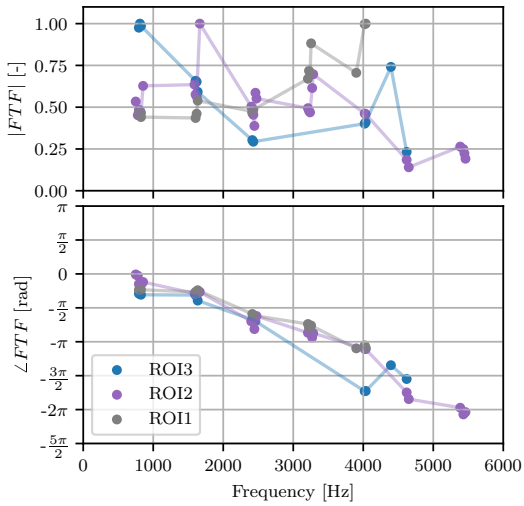

(e) LP2,LNG

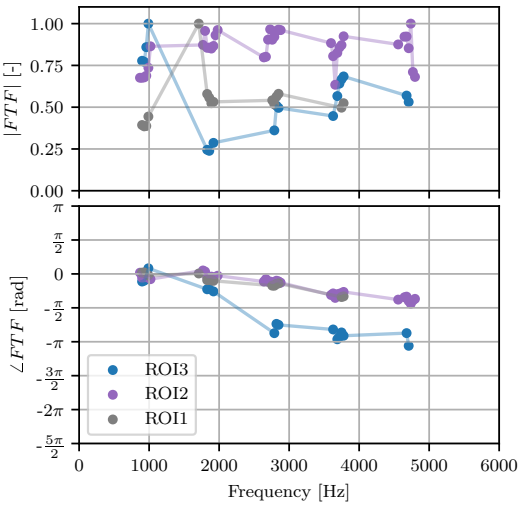

(f) LP3,LNG

Fig. 4. Flame transfer function of each LP.

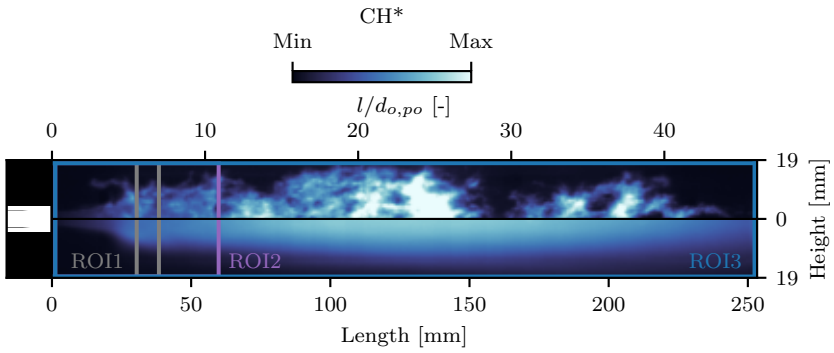

(a) LP2,H_2

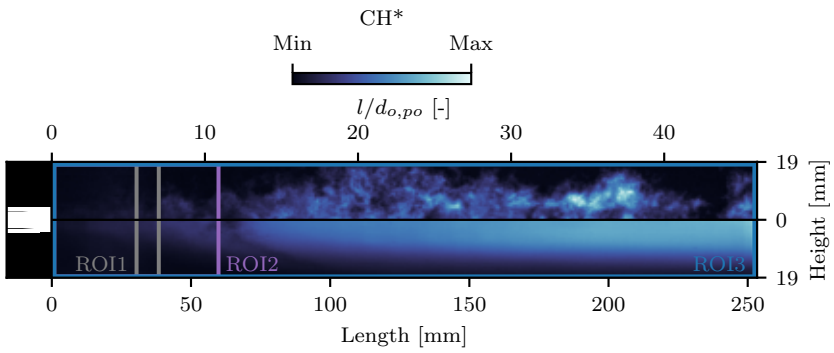

(b) Excited interval of LP1,CNG

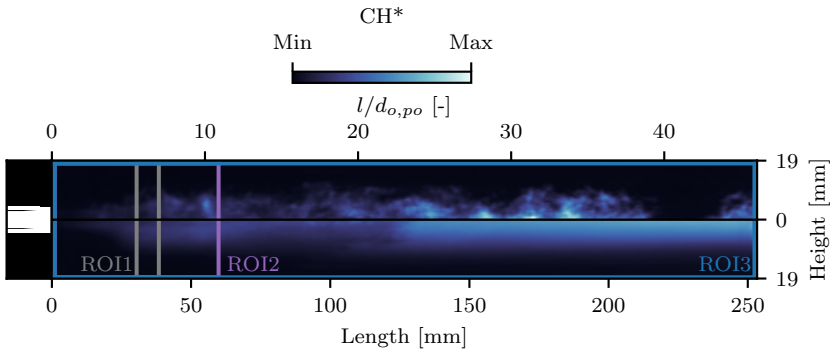

(c) LP4,LNG

Fig. 5. Instantaneous (top) and time-averaged (bottom) flame radiation imaging (CH*) for the stable and intermittent unstable LPs with ROIs for FTF calculation indicated.

tive/negative in the vicinity of the 3L frequency (Fig. 3(e)), it is clearly negative for the 4L mode (Fig. 3(e)).

4.2. Flame Transfer Function

Next the flame transfer functions (FTFs) for all six LPs will be presented. As mentioned earlier, FTFs are based on the integrated heat release response to acoustic pressure (p') or velocity (u') oscillations. Typically, determining the FTF for an experimental setup involves perturbing the injected mass flow at various frequencies and measuring the corresponding response in the heat release rate ($\dot{Q}'$).[25] However, this approach was not applicable to the experimental setup in these experiments.

Instead, the the acoustic pressure at the head end of the chamber ($p'_{cc,1}$) was used to approximate the pressure fluctuations experienced by the injected mass flow. The FTFs are calculated according to Eq. 6 using $p'_{cc,1}$ and the radiation intensity measurements, which are reduced to a 1D signal by averaging the intensity within a region of interest (ROI).

However, without explicit excitation of the injected mass flow at specific frequencies, there is a risk of obtaining non-physical high gains at certain frequencies during the calculation of FTFs. This can occur if the input signal (pressure) and the output signal (intensity) are incoherent, and a intensity fluctuation, even with low amplitude, is correlated with a negligible pressure fluctuation. To mitigate this, only gains and phases at frequencies where the coherence of the input and output signal exceeds 90% are considered.

The gain and phase of the FTFs for each LP are provided in Fig. 4. Three different ROIs are compared. The first ROI (ROI1, gray line) represents the average intensity measurements in the direct vicinity of the acoustic pressure measurement $p'_{cc,1}$, corresponding to ±4 mm axial distance from the sensor's center. The second ROI (ROI2, purple line) covers the area between injection plane and 60 mm further down-

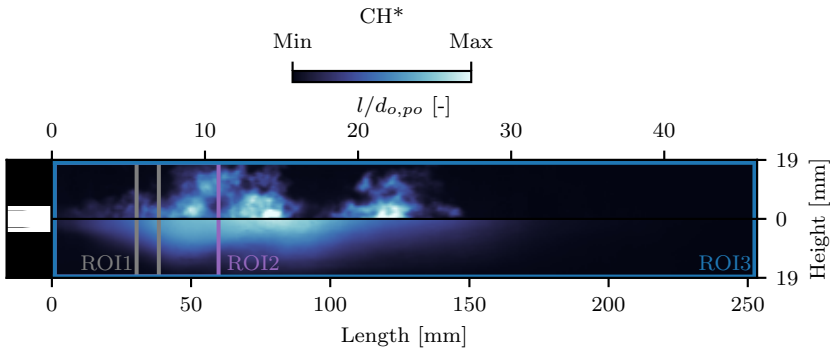

(a) LP1,LNG

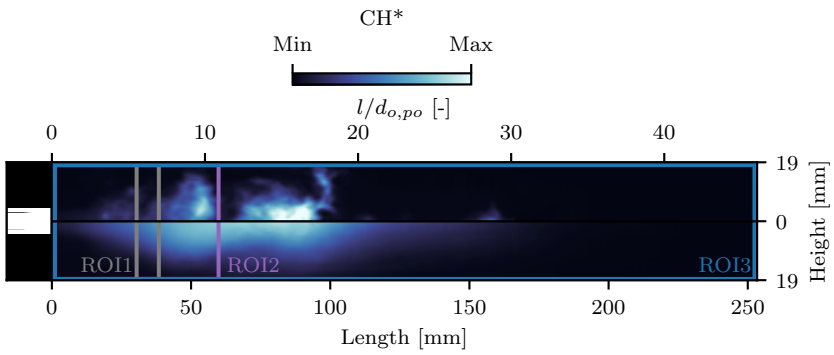

(b) LP2,LNG

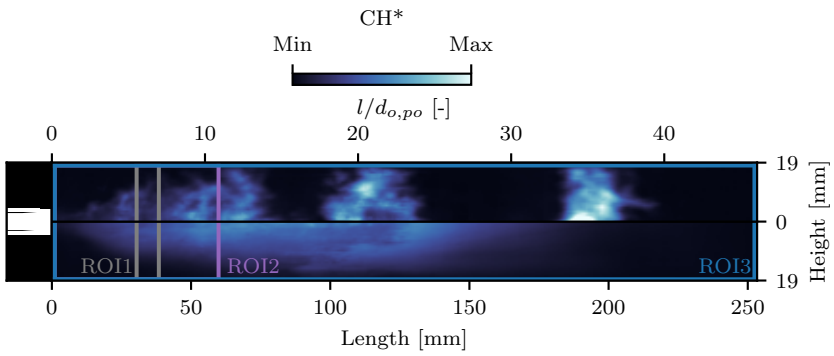

(c) LP3,LNG

Fig. 6. Instantaneous (top) and time-averaged (bottom) flame radiation imaging (CH*) for the unstable LPs with ROIs for FTF calculation indicated.

stream. This ensures that, depending on the configuration, at least up to the 3L mode the intensity measurements are extracted from the upstream part of the nodal line. Finally, the third ROI (ROI3, blue line) features an averaged intensity over the whole optical accessible region. Instantaneous and time-averaged flame radiation imaging (CH*), with the corresponding ROIs for flame transfer function calculation indicated, are provided in Fig. 5 and Fig. 6.

It should be noted here that due to a lack of an established proportionality between line-of-sight integrated radiation measurement and heat release rate, a relative comparison of the gains within a ROI for a LP are possible, but the absolute gain values are difficult to interpret. Therefore, the gain values of each FTF are normalized with the maximum gain within the same FTF. The phase of the FTFs is plotted so that negative values indicate a leading pressure signal.

As expected from the Rayleigh-Index spectra (Fig. 2(a)) there are hardly coherent frequencies for the stable LP2,H_2 (Fig. 4(a)). More specifically, for ROI1, there are no coherent frequencies. For ROI2 and ROI3 two respectively one coherent frequencies are available but at more or less arbitrary values. The same applies roughly for the second stable LP3,LNG (Fig. 4(f)). Again, only two coherent frequencies are available, but at more or less arbitrary values.

This changes for LP1,CNG (Fig. 4(b)) with an intermittent excited 1L mode. Here, pressure and intensity fluctuations are coherent near the 1L, 2L and 3L mode of the chamber for all three ROIs. However, the development of the gain is unexpected compared to the Rayleigh-Index spectra (Fig. 2(a)). One would expect to observe the highest gain at the 1L frequency. A possible explanation could be provided by the intermittent occurring instabilities preventing steady-state conditions in terms of oscillating acoustic pressure and fluctuating heat release rates from being reached. The phase difference between pressure and intensity fluctuations seems to be most reasonable for ROI3. Ideally a constant time lag among

Table 2. Time lag values

LP	P_{cc}	ROF	Time Lag [ms]	Uncertainty
2,H_2	64.3 bar	5.8	0.025	±0.05
1,CNG	66.8 bar	2.8	0.1	±0.1
1,LNG	62.9 bar	3.5	0.15	±0.05
2,LNG	65.4 bar	3.0	0.12	±0.05
3,LNG	41.3 bar	3.4	0.17	±0.1
4,LNG	40.5 bar	2.5	0.2	±0.1

all frequencies should result in a linear increasing phase lag.

Results as one would expect from the Rayleigh-Index spectra can be observed for LP4,LNG, LP1,LNG and LP2,LNG (Fig. 4(c)-4(e)). Here, at least for ROI3, the gain values of the FTF are highest for the 1L mode. Also the phase lags are in line with the findings of the Rayleigh-Index spectra. For example the Rayleigh-Index spectra for LP1,LNG (Fig. 2(d)) suggest that acoustic oscillation and heat release rate are in phase for the 1L and 2L mode, 90° phase shifted for the 3L mode and counter-phased for the modes above. This is confirmed by the phase difference of the corresponding FTF. For the 1L and 2L mode the absolute phase difference is below 90°, indicating positive coupling. At the 3L frequency, the phase lag is pretty much 90°, resulting neither in driving nor coupling. Finally the phase lags rises above 90° resulting in a negative coupling.

The averaged time lag values for extracted for each LP and ROI3 are summarized in Tab. 2. The extracted time lag values and their relation to each other are consistent with literature. LP2,H_2, which uses hydrogen as fuel, features the lowest time lag value. This is consistent with the faster reaction kinetics of hydrogen compared to natural gas respectively methane.[26] Additionally, the time lag values of the subcritical LPs using natural gas as fuel are increased compared to the supercritical LPs. This can be explained by the additional vaporization processes of subcritical injected propellants prior to reaction.[4]

It can be concluded that the used approach to determine the flame transfer functions seems to provide reasonable results if intensified excitation at certain frequencies is available. The best results in terms of gain are received for ROI3, if the whole optical accessible region is considered. The phase difference between pressure and intensity signal is pretty similar for all three ROIs.

5. Conclusion

The flame response in terms of Rayleigh-Index spectra and flame transfer functions of six different sets of operating conditions, or load points (LPs), in a single-injector rocket combustor have been examined.

For the stable LPs, positive Rayleigh-Index values could only be found in the low frequency range where broadband combustion noise is always present. In the Rayleigh-Index spectra of the LPs from intervals in which the chamber longitudinal resonance modes were excited, high integrated Rayleigh-Index values appear at the corresponding frequencies. Evaluation of the 2D-Rayleigh-Index distributions at these frequencies for one LP revealed the potential of hydrodynamics playing a role in driving the high-amplitude limit-cycle combustion instabilities.

Three different regions of interest were considered to calculate flame transfer functions for all six load points. While the phase differences between pressure and intensity signal were consistent for all three ROIs and in line with those expected from the Rayleigh-Index spectra, the gain differed. The ROI which included the intensity distribution throughout the entire optically accessible region provided the results qualitatively most consistent with that of other thermoacoustic studies in literature.

In conclusion, both the Rayleigh-Index spectra and the flame transfer functions reflect the thermoacoustic state of the sub-scale combustor well, validating the method for injector screening and generating validation data for numerical simulation.

Acknowledgments

The work is associated with DLR project of Advanced Methods for reusable Aerospace vehicle DEsign Using artificial intelligence and interdisciplinary numerical Simulation (AMADEUS) and Future Fuels. The authors would also like to thank the crew of the P8 test bench. Special thanks to Alex Grebe for his assistance in preparing and performing the experiments.

References

1) Asakawa, H., Nanri, H., Aoki, K., Kubota, I., Mori, H., Ishikawa, Y., Kimoto, K., Ishihara, S. and Ishizaki, S.: The Status of the Research and Development of LNG Rocket Engines in Japan, *Chemical Rocket Propulsion, De Luca L., Shimada T., Sinditskii V., Calabro M. (eds)*, Springer International Publishing, Switzerland, 2016, pp. 463–487.
2) Gaydon, A.G. and Wolfhard, H.G.: Flames: Their Structure, Radiation, and Temperature, Chapman & Hall, 1953.
3) Gaydon, A.G.: Hydrogen Flames, *The Spectroscopy of Flames*, Springer Dordrecht, 1974, pp. 99–126.
4) Harrje, D. T. and Reardon, F. H.: Liquid propellant rocket combustion instability , *Liquid propellant rocket combustion instability* , Scientific and Technical Information Office (NASA), 1972.
5) Rayleigh, J. W. S.: The Explanation of Certain Acoustical Phenomena, *Nature*., **18** (1878), pp. 319–321.
6) Bonciolini, G.; Faure-Beaulieu, A.; Bourquard, C. and Noiray, N.: Low order modelling of thermoacoustic instabilities and intermittency: Flame response delay and nonlinearity, *Combustion and Flame*., **226** (2021), pp. 396–411.
7) Orchini, A.; Pedergnana, T.; Buschmann, P. E.; Moeck, J. P. and Noiray, N.: Reduced-order modelling of thermoacoustic instabilities in can-annular combustors, *Journal of Sound and Vibration*., **526** (2022), pp. 116808.
8) Schulze, M. and Sattelmayer, T.: Linear Stability Assessment of a Cryogenic Rocket Engine , *International Journal of Spray and Combustion Dynamics*., **9** (2017), pp. 277–298.
9) Urbano, A.; Douasbin, Q.; Selle, L.; Staffelbach, G.; Cuenot, B.; Schmitt, T.; Ducruix, S. and Candel, S.: Study of Flame Response to Transverse Acoustic Modes from the LES of a 42-Injector Rocket Engine , *Proceedings of the Combustion Institute*., **36** (2017), pp. 2633–2639.
10) Boudy, F.; Durox, D.; Schuller, T. and Candel, S.: Nonlinear mode triggering in a multiple flame combustor, *Proceedings of the Combustion Institute*., **33** (2017), pp. 1121–1128.
11) Wierman, M.; Pomeroy, B. and Anderson, W.: Development of Combustion Response Functions in a Subscale High Pressure Transverse Combustor, *Progress in Propulsion Physics*., **8** (2016), pp. 55–74.
12) Kaufmann, A.; Nicoud, F. and Poinsot, T.: Flow forcing techniques

for numerical simulation of combustion instabilities, *Combustion and Flame*., **131** (2002), pp. 371–385.

13) Durox, D.; Schuller, T.; Noiray, N.; Birbaud, A. and Candel, S.: Rayleigh criterion and acoustic energy balance in unconfined self-sustained oscillating flames, *Combustion and Flame*., **156** (2009), pp. 106–119.
14) Richecoeur, F., Scouflaire, P., Ducruic, S. and Candel, S.: High-Frequency Transverse Acoustic Coupling in a Multiple-Injector Cryogenic Combustor, *Journal of Propulsion and Power*., **22** (2006), pp. 790–799.
15) Hardi, J. S., Beinke, S. K., Oschwald, M. and Dally, B. B.: Coupling of Cryogenic Oxygen-Hydrogen Flames to Longitudinal and Transverse Acoustic Instabilities, *Journal of Propulsion and Power*., **30** (2014), pp. 991–1004.
16) Fiala, T. and Sattelmayer, T.: Heat release and UV–Vis radiation in non-premixed hydrogen–oxygen flames, *Experiments in Fluids*., **56** (2015), article number: 144.
17) Fiala, T., Sattelmayer, T., Gröning, S., Hardi, J., Stützer, R., Webster, S. and Oschwald, M.: Comparison Between Excited Hydroxyl Radical and Blue Radiation from Hydrogen Rocket Combustion, *Journal of Propulsion and Power*., **33** (2017), pp. 490–500.
18) Sardeshmukh, S.; Bedard, M. and Anderson, W.: The use of OH* and CH* as heat release markers in combustion dynamics, *International Journal of Spray and Combustion Dynamics*., **9** (2017), pp. 409–423.
19) Martin, J.; Armbruster, W.; Stützer, R.; Suslov, D.; Hardi, J. and Oschwald, M.: Flame Dynamics of an Injection Element operated with LOX/H_2, LOX/CNG and LOX/LNG in a Sub- and Supercritical Rocket Combustor with Large Optical Access, *International Journal of Spray and Combustion Dynamics*.(2023).
20) Martin, J., Armbruster, W., Stützer, R., General, S., Knapp, B., Suslov, D. and Hardi, J.: Flame characteristics of a high-pressure LOX/H_2 rocket combustor with large optical access, *Case Studies in Thermal Engineering*., **28** (2021).
21) Martin, J.; Armbruster, W.; Suslov, D.; Stützer, R.; Hardi, J. S. and Oschwald, M.: Flame Characteristics and Response of a High-Pressure LOX/CNG Rocket Combustor with Large Optical Access, *Aerospace*., **9** (2022), pp. 410.
22) Vold, H.; Crowley, J. and Rocklin, G. T.: New ways of estimating frequency response functions, *Sound & Vibration*., **18** (1984), pp. 34-38.
23) Suslov, D., Hardi, J.S., Oschwald, M.: Full length visualization of liquid oxygen disintegration in a single injector sub-scale rocket combustor, *Aerospace Science and Technology*., **86** (2019), pp. 444–454.
24) Knab, O., Riedmann, H., Ivancic, B., Höglauer, C., Frey, M. and Aichner, T.: Consequences of modeling demands on numerical rocket thrust chamber flow simulation tools, *Progress in Propulsion Physics*., **11** (2019), pp. 317–346.
25) Durox, D.; Schuller, T.; Noiray, N. and Candel, S.: Experimental analysis of nonlinear flame transfer functions for different flame geometries, *Proceedings of the Combustion Institute*., **32** (2009), pp. 1391–1398.
26) Yang, B.; Cuoco, F. and Oschwald, M.: Atomization and Flames in LOX/H2- and LOx/CH4- Spray Combustion , *Journal of Propulsion and Power*., **23** (2007), pp. 763–771.
27) Martin, J; Armbruster, W.; Börner, M.; Hardi, J. and Oschwald, M.: Flame-Acoustic Interaction in a Sub- and Supercritical, Single-Injector, LOX/CNG/LNG Rocket Combustor with OpticalAccess, AIAA SciTech 2022 Forum, American Institute of Aeronautics and Astronautics, National Harbor, Maryland, USA, 2023.
28) Bee, A.; Börner, M.; Armbruster, W.; Knapp, B.; General, S.; Martin, J. and Hardi, J.: Experimental Study and Visualization of the Combustion Dynamics and Behavior of a Single Swirl Coaxial Injector Element in a High Pressure LOX/CH4 Rocket Combustor, AIAA SciTech 2024 Forum, American Institute of Aeronautics and Astronautics, Orlando, Florida, USA, 2024.
29) Tsohas, J. and Heister, S.: Prometheus: CFD Simulations of Liquid Rocket Coaxial Injector Hydrodynamics, 45th AIAA/ASME/SAE/ASEE Joint Propulsion Conference & Exhibit, American Institute of Aeronautics and Astronautics, Denver, Colorado, USA, 2009.
30) Schmid, M. and Sattelmayer, T.: Interaction of Acoustic Pressure Fluctuations with Supercritical Nitrogen Jets , 48th AIAA/ASME/SAE/ASEE Joint Propulsion Conference & Exhibit, American Institute of Aeronautics and Astronautics, Atlanta, Georgia, USA, 2012.
31) Beinke, S. K.: Anaylses of Flame Response to Acoustic Forcing in a Rocket Combustor, Ph.D. Thesis, The University of Adelaide, 2017.
32) Freitag, E.: On the Measurement and Modelling of Flame Transfer Functions at Elevated Pressure , Ph.D. Thesis, Technical University of Munich, 2009.
33) Schulze, M.: Linear Stability Assessment of Cryogenic Rocket Engines, Ph.D. Thesis, Technical University of Munich, 2016.